Article

Structure

Molecular Basis of MgATP Selectivity of the Mitochondrial SCaMC Carrier

Highlights

- Developed high-resolution NMR system for the MgATP/Pi transporter
- Achieved NMR resonance assignment for the 292-residue transporter
- Identified the MgATP binding site in the transporter
- Identified a key residue for SCaMC's selectivity for MgATP over ATP

Authors

Changqing Run, Qin Yang, Zhijun Liu, Bo OuYang, James J. Chou

Correspondence

james_chou@hms.harvard.edu (J.J.C.), ouyang@sibcb.ac.cn (B.O.)

In Brief

The AAC and SCaMC are two major nucleotide carriers responsible for transporting ATP/ADP and metal-complexed ATP/ADP across the mitochondrial inner membrane. Run et al. reveal key structural difference between the two homologs, which explains SCaMC's higher selectivity for transporting MgATP over ATP compared with AAC.

Run et al., 2015, Structure *23*, 1394–1403
August 4, 2015
http://dx.doi.org/10.1016/j.str.2015.06.004

CellPress

CellPress

Structure
Article

Molecular Basis of MgATP Selectivity of the Mitochondrial SCaMC Carrier

Changqing Run,[1,2] Qin Yang,[3] Zhijun Liu,[1] Bo OuYang,[1,2,*] and James J. Chou[1,2,3,*]
[1]National Center for Protein Science, Shanghai Institute of Biochemistry and Cell Biology, Chinese Academy of Sciences, Shanghai 200031, China
[2]State Key Laboratory of Molecular Biology, Shanghai Institute of Biochemistry and Cell Biology, Chinese Academy of Sciences, Shanghai 200031, China
[3]Department of Biological Chemistry and Molecular Pharmacology, Harvard Medical School, Boston, MA 02115, USA
*Correspondence: james_chou@hms.harvard.edu (J.J.C.), ouyang@sibcb.ac.cn (B.O.)
http://dx.doi.org/10.1016/j.str.2015.06.004

SUMMARY

The mitochondrial matrix is the supplier of cellular ATP. The short Ca^{2+}-binding mitochondrial carrier (SCaMC) is one of the two mitochondrial carriers responsible for transporting ATP across the mitochondrial inner membrane. While the ADP/ATP carrier (AAC) accounts for the bulk ADP/ATP recycling in the matrix, the function of SCaMC is important for mitochondrial activities that depend on adenine nucleotides, such as gluconeogenesis and mitochondrial biogenesis. A key difference between SCaMC and AAC is that SCaMC selectively transports MgATP whereas AAC only transports free nucleotides. Here, we use a combination of nuclear magnetic resonance experiments and functional mutagenesis to investigate the structural basis of the MgATP selectivity in SCaMC. Our data revealed an MgATP binding site inside the transporter cavity, while identifying an aspartic acid residue that plays an important role in the higher selectivity for MgATP over free ATP.

INTRODUCTION

Mitochondria play vital roles in energy metabolism of the cells and supply most of the ATP, the energy currency in life (Huss and Kelly, 2005). Selective transport of ATP and ADP into and out of the mitochondrial matrix is catalyzed by two nucleotide carriers, which belong to the large family of mitochondrial carriers that transport various metabolites, nucleotides, and vitamins across the inner mitochondrial membrane. The ADP/ATP carrier (AAC) is the major carrier that exports ATP out of the matrix for energy consumption while importing ADP for the production of new ATP by the ATP synthase (Fiore et al., 1998; Klingenberg, 2008). Functional defects of AAC can be detrimental. For example, defective mutations in the AAC lead to the Sengers syndrome (Palmieri, 2008). Another carrier that transports ATP is the short Ca^{2+}-binding mitochondrial carrier (SCaMC) (Chen, 2004; del Arco and Satrustegui, 2004; Fiermonte et al., 2004). While AAC accounts for the bulk ADP/ATP recycling in the matrix, the transport activity of SCaMC is important for mitochondrial activities in the matrix that depend on adenine nucleotides, such as gluconeogenesis and mitochondrial biogenesis (Aprille, 1988; Pollak and Sutton, 1980; Satrústegui et al., 2007; Schild et al., 1999; Traba et al., 2012).

The transport properties of SCaMC, however, are very different from those of the AAC. First, the transport activity of SCaMC is Ca^{2+} dependent, i.e., SCaMC remains inactive unless stimulated by a cytosolic Ca^{2+} signal (Nosek et al., 1990; Pollak and Sutton, 1980). SCaMC adopts, in addition to the transmembrane domain (TMD) that is homologous to the AAC, an extramembrane N-terminal domain (NTD) that contains four EF-hand motifs in a calmodulin-like arrangement (Fiermonte et al., 2004; Satrústegui et al., 2007; Yang et al., 2014). Previous structural and biochemistry data suggest a capping/uncapping mechanism by which the apo NTD caps the TMD cavity from the intermembrane space of mitochondria and blocks substrate transport, whereas Ca^{2+} binding converts NTD to a self-sequestered form that uncaps the cavity (Cavero et al., 2005; Chen, 2004; Yang et al., 2014).

Another key difference between AAC and SCaMC is in the substrate selectivity of the TMD. Unlike the AAC that selectively transports free ADP or ATP (Nury et al., 2006), the TMD of SCaMC ($SCaMC_{TMD}$) transports MgATP in exchange for phosphate (Pi). It has been shown that the $SCaMC_{TMD}$ has much higher selectivity for MgATP than for free ATP, although it can also transport ATP (Austin and Aprille, 1984; Fiermonte et al., 2004; Pollak and Sutton, 1980). Earlier in vivo studies in rat liver mitochondria show that the ATP uptake can be enhanced in the presence of Mg^{2+} and is significantly depressed in the absence of Mg^{2+} (Austin and Aprille, 1984; Pollak and Sutton, 1980). In vitro studies by reconstituting recombinant SCaMCs and measuring the uptake of [^{14}C]ADP or [^{33}P]Pi into proteoliposomes have shown a greater activity for MgATP than ATP (Fiermonte et al., 2004).

To date, the only high-resolution crystal structures of mitochondrial carriers are those of AAC in complex with the inhibitor carboxyatractyloside (CATR) (Figure 1A) (Pebay-Peyroula et al., 2003; Ruprecht et al., 2014). In addition to the AACs, the backbone structure of the Uncoupling Protein 2 (UCP2), another mitochondrial carrier, has been characterized using nuclear magnetic resonance (NMR) in the presence of guanosine diphosphate (GDP) (Berardi et al., 2011). In the case of UCPs, GDP is not a transporting substrate but rather an inhibitor that inhibits the fatty

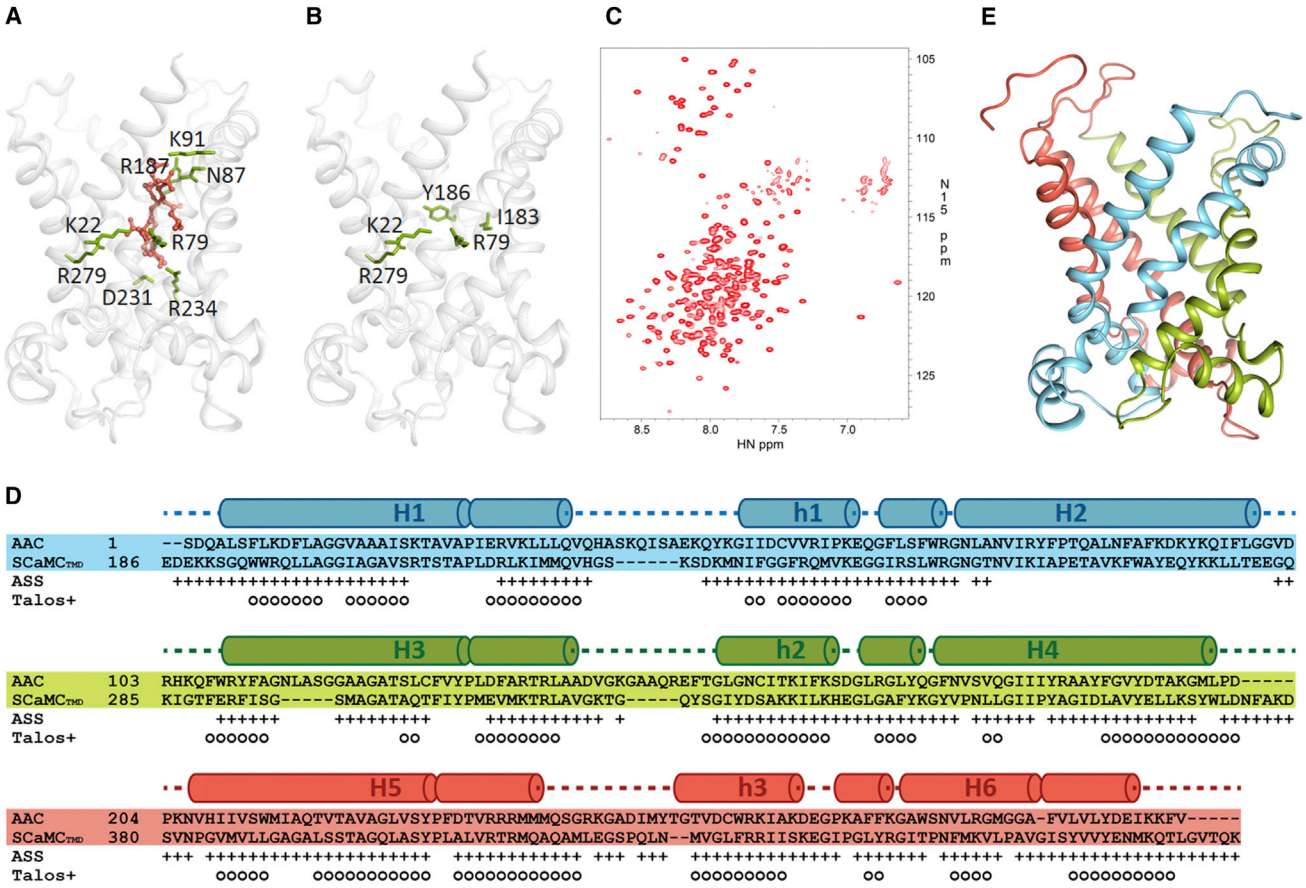

Figure 1. NMR Characterization of the AAC-Homologous Domain of SCaMC

(A) The crystal structure of AAC in complex with the inhibitor CATR (PDB: 1OKC). CATR is shown as sticks and balls in red. AAC residues interacting with CATR are shown as green sticks.

(B) Proposed ATP binding site in AAC based on functional mutagenesis. The ATP pyrophosphate binds to K22, R79, and R279 (green sticks).

(C) The ^{1}H-^{15}N TROSY-HSQC spectrum of 0.4 mM *U*-[^{15}N, ^{13}C, ^{2}H]SCaMC$_{TMD}$ in the presence of 60 mM DPC recorded at 30°C and 600 MHz.

(D) Backbone assignments and secondary structures of SCaMC$_{TMD}$. Alignment between AAC and SCaMC$_{TMD}$ is the same as in Figure S1. Secondary structures of AAC are indicated as cylinders and labeled as H1–H6 (TM helices) and h1–h3 (amphipathic helices). The assigned residues of SCaMC$_{TMD}$ are indicated as '+.' Helical regions predicted by the assigned chemical shifts (Talos+) (Shen et al., 2009) are indicated as 'o.'

(E) Homology model of SCaMC$_{TMD}$ made using Modeller 9 based on the sequence alignment in (A) and the crystal structure of bovine AAC.

acid flipping activity of UCPs (Berardi and Chou, 2014; Garlid et al., 1996). UCP2 has ~20% sequence identity with AAC, and the NMR structure shows that UCP2 has overall architecture very similar to that of AAC (Berardi et al., 2011). In both cases, the structure features six severely kinked transmembrane (TM) helices packed to form a barrel that is open to the intermembrane space. The structures also show three structurally similar domains arranged in quasi 3-fold symmetry, with each domain consisting of two TM helices and an amphipathic helix between them on the matrix side.

Although there are no structures showing the binding of substrate to AAC, possibly due to weak substrate binding and the dynamic nature of the uninhibited states of the carriers, extensive mutagenesis data suggest that the binding residues are located in the middle of the cavity including Lys22, Arg79, Arg279, Gly182, Ile183, and Tyr186 (Kunji and Robinson, 2006; Nury et al., 2006), among which the conserved Lys22, Arg79, and Arg279 form salt bridges with phosphates of ATP (Figure 1B). The SCaMC$_{TMD}$ has 27%–30% sequence identity with AAC (Fiermonte et al., 2004) and is also expected to have architecture similar to that of AAC. Moreover, these basic residues that have been proposed to be involved in ADP/ATP binding in AAC are also conserved among the SCaMC sources. The alignment of the key basic residues between AAC and SCaMC$_{TMD}$ (Figure S1) is consistent with the observation that the SCaMC can also transport free ADP or ATP. However, there are no clues as to how SCaMC$_{TMD}$ achieves strong selectivity for MgATP over free ATP.

In this study, we used a combination of NMR and functional mutagenesis to investigate the binding of MgATP to the SCaMC$_{TMD}$. NMR measurements identified locations of specific MgATP binding. Functional mutagenesis of the substrate binding sites observed by NMR further identified a key aspartic acid residue inside the cavity that is critical for MgATP transport and for the selectivity for MgATP over ATP. In addition to MgATP binding, our NMR data also suggest that the SCaMC$_{TMD}$ is structurally homologous to the AAC.

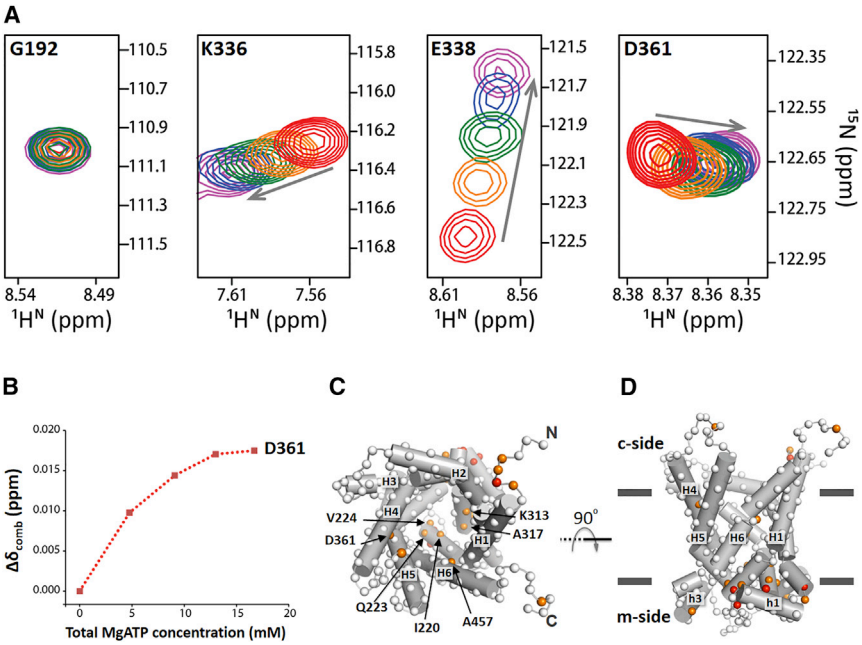

Figure 2. Chemical Shift Perturbations Induced by MgATP Binding

(A) MgATP titrations showing residue-specific and concentration-dependent chemical shift changes. The peaks are from 2D ^{1}H-^{15}N TROSY-HSQC spectra recorded with a 0.4 mM *U*-[^{15}N, ^{13}C, ^{2}H] sample. The spectra were recorded in the presence of 0 mM (red), 4.8 mM (yellow), 9.1 mM (green), 13.0 mM (blue), and 16.7 mM (purple) MgATP.

(B) Plots of $\Delta\delta_{comb}$ (defined in Equation 2) versus MgATP concentration for residues D361 in (A).

(C and D) Comprehensive $\Delta\delta_{comb}$ mapping onto the homology model of SCaMC$_{TMD}$ using NMR titration data obtained from 3D TROSY HNCO spectra recorded at 600 MHz. Residues with $\Delta\delta_{comb} > 0.030$ ppm are shown in red and those with $0.015 < \Delta\delta_{comb} < 0.030$ ppm are shown in orange.

Arrows in (A) indicate the direction of resonance movements upon addition of the substrate. Arrows in (C) indicate the cavity-lining residues.

RESULTS

The TM Domain of SCaMC Adopts a Structural Fold Similar to that of AAC

We first established an NMR-amenable and functionally relevant sample of SCaMC$_{TMD}$ for investigating substrate binding. The TMD of human SCaMC (residues 186–477) was expressed in *Escherichia coli* cells, reconstituted in dodecylphosphocholine (DPC) micelles, and purified by Ni-NTA affinity and size-exclusion chromatography (see Experimental Procedures). The final NMR sample, which contains 0.4 mM SCaMC$_{TMD}$, 60 mM DPC, 20 mM 2-(*N*-morpholino)ethanesulfonic acid (MES) (pH 6.5), shows NMR spectra with good resolution and resonance homogeneity (Figure 1C). Using three pairs of triple-resonance experiments and 3D double ^{15}N-edited nuclear Overhauser effect spectroscopy (NOESY), we could assign ~80% of the backbone resonances of non-proline residues (Figure 1D). The majority of the unassigned residues are in the region from Asn257 to Phe289, possibly due to exchange broadening. The mitochondrial carrier proteins have intricate and unique arrangement of helical segments that features six long TM helices with short breaks and three amphipathic helices (Berardi et al., 2011; Pebay-Peyroula et al., 2003; Ruprecht et al., 2014; Sounier et al., 2015). Using sequence alignment and the crystal structure of AAC, we generated a homology model of the SCaMC$_{TMD}$ using the program Modeller 9 (Figure 1E) (Webb and Sali, 2014). It should be noted that the original AAC structure was solved in the complex with an inhibitor CATR (Pebay-Peyroula et al., 2003), so the structural model may not accurately reflect that of the free SCaMC$_{TMD}$. Nonetheless, the model provides a structural framework for elucidating substrate binding of this MgATP carrier.

The SCaMC$_{TMD}$ Binds Specifically to MgATP and ATP

It has been reported that the substrates of SCaMC include MgATP, ATP, ADP, AMP, and Pi (Aprille, 1988; Austin and Aprille, 1984; del Arco and Satrustegui, 2004; Fiermonte et al., 2004; Joyal and Aprille, 1992). We first performed NMR titration experiments to characterize the interactions between SCaMC$_{TMD}$ and substrates. To measure substrate-induced chemical shift perturbations, SCaMC$_{TMD}$ sample was titrated with MgATP or ATP as well as free Mg^{2+} solubilized in the NMR buffer. The MgATP titration showed residue-specific and concentration-dependent chemical shift perturbations (Figures 2A, 2B, and S2). Moreover, addition of free ATP to the sample induced chemical shift changes similar to those induced by MgATP (Figure S2). This result is consistent with previous functional measurement that both MgATP and ATP are substrates of SCaMC (Austin and Aprille, 1984; Fiermonte et al., 2004; Pollak and Sutton, 1980). Although MgATP and ATP show specific binding, the Mg^{2+} ion alone induces little chemical shift changes (Figure S2), which is also consistent with the fact that Mg^{2+} alone is not a substrate of SCaMC.

We further examined MgATP interaction by titrating a *U*-[^{15}N, ^{13}C, ^{2}H] sample using the 3D transverse relaxation optimized spectroscopy (TROSY) HNCO experiment. The chemical shift changes induced by MgATP are located at multiple parts of the protein. As expected from the general model that substrates bind inside the cavity of mitochondrial carriers, several cavity-lining residues show strong perturbations, including Ile220, Gln223, Val224, Lys313, Ala317, Asp361, and Ala457 (Figure 2C). In addition to the cavity, however, we observed strong chemical shift changes located both at the cytosol-facing mouth of the cavity and on the matrix side of the carrier (Figure 2D). The perturbed residues near the cavity mouth include the N-terminal residues (Glu188, Lys189, Lys190, and Ser191), and Lys378 and Gln476. The perturbed residues on the matrix side include residues of H1 and H3 near the matrix end of the cavity and residues of the amphipathic helices h1 and h2. We note that the chemical shift change is potentially complicated by the possible equilibrium exchange between

the presumed c and m states, i.e., the substrate may interact with the two states differently.

Among the perturbed residues, Asp361 shows relatively fast binding saturation. By comparing the MgATP titration data of Asp361 with the simulated binding curves for 0.4 mM protein concentration at different K_D values, the apparent K_D at Asp361 is estimated to be between 1 and 2 mM (Figure S3).

Direct Identification of Substrate Binding Sites Using Paramagnetic Probe

Chemical shift perturbation is an indirect indication of substrate binding because it could have arisen from substrate directly and/or binding-induced conformational change. To directly probe substrate binding sites of $SCaMC_{TMD}$, we used Mn^{2+}, a paramagnetic ion, to replace Mg^{2+}. Mn^{2+} is similar to Mg^{2+}; it has often been used as an Mg^{2+} substituent in many Mg^{2+}-dependent enzymatic reactions (Cathala and Brunel, 1975; Guth and Burris, 1983; Hsu and Berg, 1978; Ohshima et al., 2008). Paramagnetic relaxation enhancements (PREs) have been demonstrated to be very useful for investigating membrane proteins (Barrett et al., 2012; Berardi and Chou, 2014; Zhang et al., 2015). In this experiment, we used the 3D TROSY HNCO experiment that correlates the chemical shifts of backbone ^{1}H, ^{15}N, and ^{13}C nuclides to measure resonance broadening due to the PRE induced by the Mn^{2+}. Addition of 1.25 mM MnATP to a 0.4 mM $SCaMC_{TMD}$ sample resulted in a wide range of resonance broadening (Figure 3A). The intensity of some resonances decreased by more than 70%. Most of these resonances are located in the loop of the cytosol-facing side of the cavity and on the amphipathic helices on the matrix side of $SCaMC_{TMD}$ (Figure 3B). Only a small fraction of the affected residues are in the central cavity.

The divalent cations such as Mg^{2+} and Mn^{2+} are known to interact with phospholipids and acidic residues, resulting in nonspecific binding. To separate the specific from nonspecific effects, we employed displacement titration, which involves first broadening the protein NMR peaks by the paramagnetic MnATP (1.25 mM) and then measuring specific recovery of the peaks upon incremental addition of the non-paramagnetic MgATP. In this case, the rapidly recovered peaks should in principle correspond to regions where MgATP specifically competes off MnATP and the rate of recovery should reflect the relative binding affinity at these sites. The intensity recovery can be described mathematically as

$$\Delta I = \Delta I_{max} \frac{[\mathrm{MgATP}]}{K'_D + [\mathrm{MgATP}]}, \qquad \text{(Equation 1)}$$

where ΔI is the intensity recovery at a given MgATP concentration, ΔI_{max} represents the maximum intensity recovery, and K'_D denotes the apparent displacement constant. More specifically, intensity recovery in the presence of MnATP is the difference between the normalized peak intensity at a given MgATP concentration (I) and that at no MgATP (I_0), where the normalized peak intensity is defined as (peak height)/(reference peak height without MnATP or MgATP). For each of the displacement titration points ranging from 0 to 22.2 mM of MgATP, a 3D TROSY HNCO spectrum was recorded (Figure 3C) to measure peak heights. The I versus [MgATP] data were then fit to Equation 1 to derive the K'_D and ΔI_{max} of each of the assigned residues (Table 1).

We found that only a small subset of the broadened peaks recovered with a well-defined displacement saturation profile (Figure 3D) that could be fitted to Equation 1. For example, the peak for Gly359, which almost vanished in the presence of MnATP, recovered rapidly upon addition of MgATP, whereas the peak for Gly429, which was also significantly reduced to 40%, did not recover. Highlighting the residues that show significant PRE (I_0<0.3), significant peak intensity recovery (ΔI_{max}>0.3), and fast displacement (K'_D<2.5 *mM*) (Table 1) in the structural model of the $SCaMC_{TMD}$ reveals a cluster of residues. They include residues Gly359, Asp361, Leu362, and Ala363 of H4, shown in Figure 3E and labeled as site I. In addition to the above residues, which form the most obvious binding patch inside the cavity, several residues in the loop between H4 and H5, Asp374, Asn375, Phe376, and Ala377, at the mouth of the cavity, also show low K'_D values, labeled as site II (Figure 3E). The overall results obtained using the paramagnetic probe suggest that the MgATP binding sites are in sites I and II of the protein.

To exclude the possibility that the PREs were caused by Mn^{2+} instead of MnATP and that Mn^{2+} was displaced by Mg^{2+} rather than MgATP, we also performed titration using Mn^{2+} and Mg^{2+}. In the presence of 1.25 mM Mn^{2+}, there are PRE effects for a few residues mainly located near the mouth of the cavity and the matrix side. Among the resolved peaks, the height of 11 peaks decreased by more than 90%. However, adding increasing amounts of Mg^{2+} did not result in peak intensity recovery (Figure S4), suggesting that the PREs from Mn^{2+} in these cases are mostly due to nonspecific partitioning of the divalent cations at the phospholipid headgroups. This negative control is a further confirmation that the residues of sites I and II in Figure 3E are specific binding sites for MgATP.

The NMR-Derived Substrate Binding Site Is Critical for MgATP Selectivity

Of the two binding sites observed by NMR, one is inside the cavity, which is anticipated based on earlier functional data, and the other is outside the cavity and unexpected. It is thus important to examine whether the two binding sites are functionally relevant. We developed a liposome-based transport assay for measuring MgATP and ATP transport by $SCaMC_{TMD}$ (Figure 4A). In this assay, the $SCaMC_{TMD}$ used for the NMR experiments is reconstituted into liposomes with Pi present in both internal and external buffers. Substrate transport is initiated by the addition of MgATP or ATP to the external solution, followed by monitoring the transporter-mediated influx of ATP or MgATP using the luciferase reporter. It has been reported that SCaMC transports MgATP much faster than ATP (Fiermonte et al., 2004; Nury et al., 2006). Indeed, our liposome experiments show that in the same time duration, the $SCaMC_{TMD}$ proteoliposome on average transports two to five times as much MgATP as ATP (Figures 4B and S5), and this result is consistent with previous reports that SCaMC has a 2- to 3-fold higher selectivity for MgATP over ATP (Austin and Aprille, 1984; Fiermonte et al., 2004; Pollak and Sutton, 1980).

Having established a quantitative assay that recapitulates the hallmark of SCaMC function, i.e., strong selectivity for MgATP

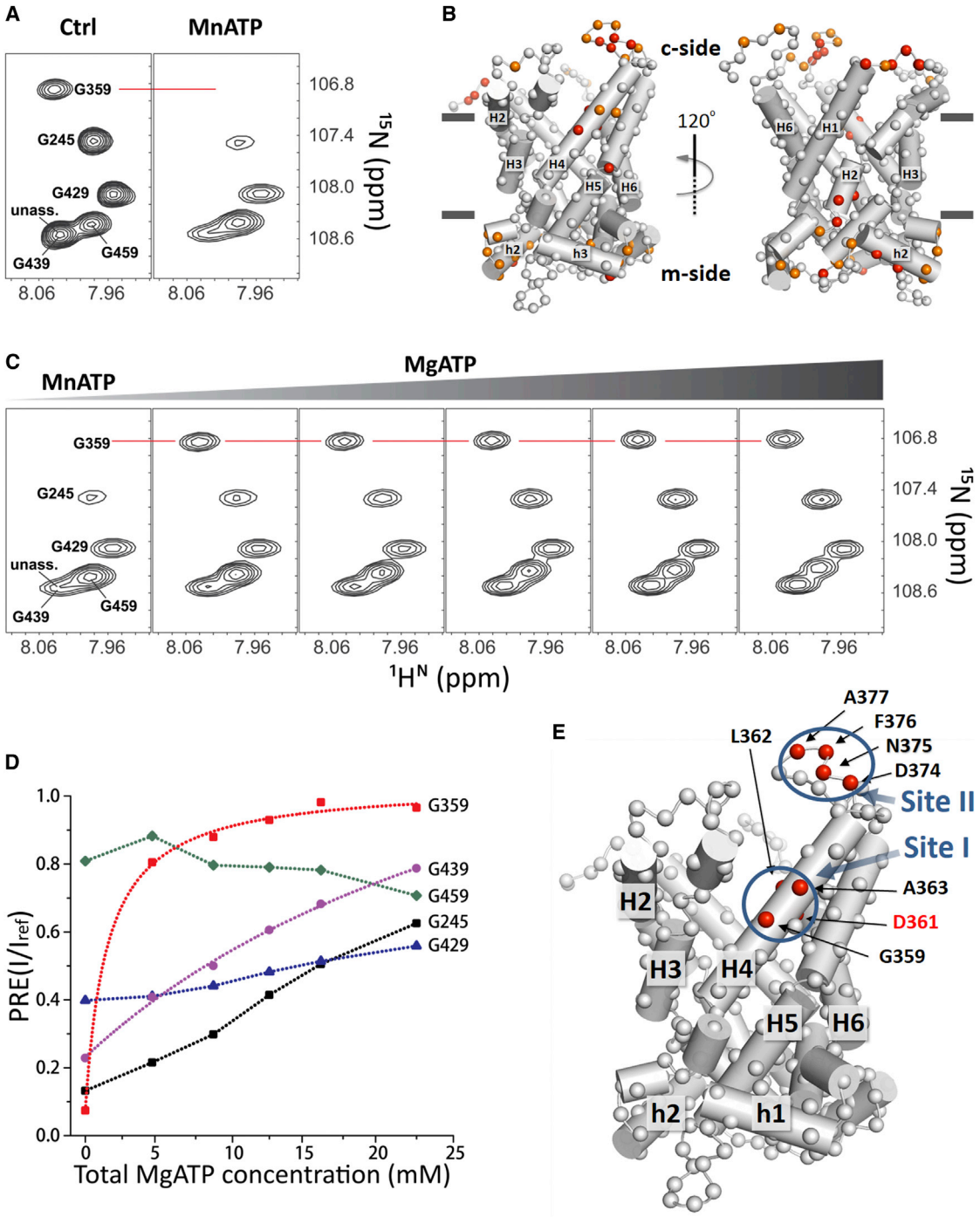

Figure 3. Direct Identification of Substrate Binding Sites Using Paramagnetic Probe

(A) A region of 2D ^{1}H-^{15}N TROSY-HSQC spectra of SCaMC$_{TMD}$ showing PRE effects of MnATP. Left and right panels correspond to spectra recorded with a 0.4 mM protein sample in the absence and presence of 1.25 mM MnATP, respectively.

(B) Mapping of MnATP-induced PRE onto the SCaMC$_{TMD}$ model. Peak intensities decreased by more than 90% are shown in red and those decreased between 70% and 90% are shown in orange.

(C) The intensity recovery of broadened peaks by addition of MgATP. The first panel shows the same spectral region as the right panel in (A). Panels 2–6 are spectra recorded at increasing concentrations of 4.5, 8.69, 12.5, 16.0, and 22.2 mM MgATP.

(D) Plots of PRE (normalized peak intensity) versus MgATP concentration for the residues labeled in (A). The peak intensity recovery data of only G359 and G439 could be fitted to the binding displacement equation (Equation 1).

(E) Mapping of significant PREs that could be specifically reduced by MgATP (I_0<0.3, ΔI_{max}>0.3 and K'_D<2.5 mM) (shown in red) onto the SCaMC$_{TMD}$ model. Red lines in (A) and (C) are indications of the location of peak G359.

Table 1. MnATP-Induced PREs and Specific Displacement of MnATP by MgATP

Residue	I_0[a]	ΔI_{max}[b]	K'_D (mM)[c]
Gly359	0.070	0.9630	1.4891
Asp361	0.044	0.5555	1.2311
Leu362	0.047	0.5515	0.4143
Ala363	0.115	0.5455	0.1985
Asp374	0.050	0.5898	1.3272
Asn375	0.036	0.5775	2.2822
Phe376	0.132	0.6129	0.3267
Ala377	0.169	0.5507	0.0498

[a]Normalized peak intensity in the presence of 1.25 mM MnATP without MgATP.
[b]Maximum peak intensity recovery as MnATP is displaced with MgATP.
[c]Apparent displacement constant in Equation 1.

over ATP, we next used the assay to carry out functional mutagenesis to examine whether newly identified residues play a role in this unique functional property of $SCaMC_{TMD}$. Since acidic residues are known to interact with divalent cations, an obvious suspect is Asp361, which is approximately at the center of site I and is completely conserved throughout SCaMC. Another suspect is Asp374, which is a part of site II, although this residue is not well conserved in SCaMC. We tested the effect of single mutations D361Y and D374A on the function of $SCaMC_{TMD}$. The Asp361 was mutated to tyrosine because the corresponding amino acid at this residue position in AAC is tyrosine.

The two single mutants were purified following the same protocol; their TROSY heteronuclear single-quantum coherence (HSQC) spectra overlap very well except for modest chemical shift changes around the mutated residues (Figure S6), indicating that the mutations did not change the carrier conformation. The liposome assays were performed to measure the effect of the mutations on the ratio of the rate of MgATP transport to that of ATP transport. The D374A mutant shows a ratio similar to that of the wild-type (WT) (Figure 4B; Table 2). The D361Y mutation, however, dramatically reduced the selectivity for MgATP over free ATP as the ratio decreased from 4.4 to 1.1 (Figure 4B; Table 2). We note that the D361Y mutant still shows transport activity for the free ATP similar to that of the D374A mutant (Table 2), suggesting that the abilities of the two mutants to transport nucleotides are similar. The major difference is the large reduction in selectivity for MgATP.

To further test the direct role of Asp361 in MgATP binding, we examined whether the single mutant D361A can still bind MgATP using the MnATP/MgATP displacement method. Addition of 1.25 mM MnATP caused similar PRE for glycines 245, 429, 439, and 459, as in the WT, but the resonance of Gly359, which showed 90% intensity reduction in the WT, decreased only by ~30% and did not show peak intensity recovery when titrating with MgATP (Figure S7). This result indicates that the D361A mutation has essentially abrogated MgATP binding to site I.

DISCUSSION

The NMR titration and functional mutagenesis data revealed Asp361 of site I as a key residue for the $SCaMC_{TMD}$ to achieve ~4-fold higher selectivity for MgATP over free ATP. Based on the structural model of $SCaMC_{TMD}$ shown in Figure 3E, Asp361 is inside the polar cavity of the carrier and is slightly closer to the cytoplasmic side than the matrix side. This model was built based on the assumption that $SCaMC_{TMD}$ and AAC have similar tertiary structures. We believe this to be a good assumption for two reasons. First, among the mitochondrial carriers, the $SCaMC_{TMD}$ is one of the closest sequence homologs of AAC with ~30% sequence identity; it is also the closest functional homolog of AAC, as it can transport ADP and ATP. Second, the AAC has an intricate arrangement of helical segments. The fact that the helical segments of the $SCaMC_{TMD}$ agree well with those of AAC is an indication that its overall architecture is similar to that of AAC. Another issue is that the AAC structure after which the model was built is in the CATR-bound state, which represents a state in which the central cavity is accessible from the intermembrane space or the cytosolic side (denoted as the c state). According to previous functional studies, the AAC in isolated mitochondria is predominantly in the c state even in the absence of the inhibitor (Klingenberg, 2008). We therefore believe that the $SCaMC_{TMD}$ model derived from the NMR data and sequence alignment is a good model for guiding mutagenesis and elucidating substrate binding.

The MgATP binding site inside the cavity was identified directly based on the PREs induced by the paramagnetic MnATP and reduced PREs due to displacement of MnATP by MgATP. But when titrating the $SCaMC_{TMD}$ with MgATP, several residues on the matrix side of the carrier, which did not show PRE recovery, showed significant chemical shift changes. Specifically, these residues belong to the matrix ends of H1 and H3 and amphipathic helices h1 and h2. The global chemical shift perturbation suggests that MgATP binding inside the cavity can allosterically affect the conformation and/or dynamics of the matrix part of the carrier. This type of allostery is possible for the carriers because substrate binding should facilitate the conformational switch from the c state described above to the m state, in which the cavity is accessible from the matrix side. In this case, the conformational switch should involve rearrangements of the amphipathic helices and opening of the matrix side of the cavity.

The NMR measurements identified two major binding sites for MgATP (Figure 3E). Site I, which is the higher-affinity site (average K'_D ~830 μM), contains residues Gly359, Asp361, Leu362, and Ala363, and is inside the polar cavity. The lower-affinity site II (average K'_D ~1,000 μM) contains residues Asp374, Asn375, Phe376, and Ala377, in a loop near the mouth of the cavity. We emphasize that although our NMR titration data provide evidence for these two sites, there could be other unidentified sites involving residues whose resonances could not be assigned. The majority of unassigned residues are between Arg209 and Asp216 (the center of H1), Asn257 and Phe289 of H2, and Phe305 and Met309 (the center of H3). The residues of site I are highly conserved whereas the residues of site II are not, suggesting that site I is the functionally important one. Furthermore, our functional mutagenesis experiments showed that mutating Asp361 of site I to tyrosine eliminates its selectivity for MgATP over ATP, but introducing the D374A mutation in site II does not significantly affect the MgATP selectivity. Although Asp374 in site II appears to be less important, it could

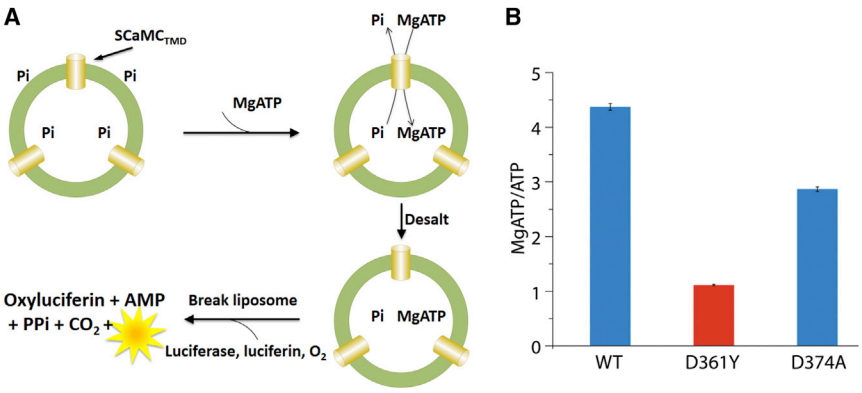

Figure 4. Effects of Mutating MgATP Binding Sites on MgATP Selectivity

(A) Schematic illustration of the liposome assay for measuring SCaMC$_{TMD}$ transport of MgATP and free ATP (details described in Experimental Procedures).

(B) Ratios of transport rate of MgATP to that of free ATP for the WT SCaMC$_{TMD}$ and its D374A and D361Y mutants. The transport rate is quantified with the total ATP transported into the liposome in 5 min. Error bars are ±1 SD values determined from three repeat measurements.

play a secondary role in recruiting the substrate to the transporter via charge-charge interaction.

SCaMC$_{TMD}$ can transport MgATP whereas AAC cannot. Since their structures are homologous, comparing the cavity-lining residues between AAC and SCaMC$_{TMD}$ can thus provide insights as to how Asp361 plays a critical role in introducing the MgATP selectivity to SCaMC$_{TMD}$. Previous studies suggest that the ATP binding residues in AAC are located in the middle of the cavity including Lys22, Arg79, Arg279, Ile183, and Tyr186 (Kunji and Robinson, 2006; Nury et al., 2006). These residues are also conserved in SCaMC$_{TMD}$ as Arg209, Lys260, Lys453, Ile354, and Tyr357, respectively (Figures 5A and 5B). Among these, the conserved basic residues such as Lys22, Arg79, and Arg279 in AAC have been proposed to form salt bridges with pyrophosphates of ATP. We believe that the corresponding basic residues Arg209, Lys260, and Lys453 allow SCaMC$_{TMD}$ to bind and transport free ATP like AAC.

A major difference between SCaMC$_{TMD}$ and AAC is that the Asp361 central to site I of SCaMC$_{TMD}$ is Tyr190 in AAC (Figure 5C), although the regions around the two residues are very similar (e.g., the tyrosine three residues before and after Asp361). Tyr186, Tyr190, and Tyr194 in AAC form a tyrosine ladder, which has been proposed to play a role in substrate recognition (Dehez et al., 2008; Nury et al., 2006; Pebay-Peyroula et al., 2003). It is thus conceivable that the Asp361 in SCaMC$_{TMD}$ has the effect of increasing affinity for MgATP at this position because aspartic acid is often involved in binding to divalent cations, i.e., Asp361 might coordinate Mg^{2+} together with the phosphate groups of ATP as illustrated in Figure 5D. Although there may be other structural features developed in SCaMC$_{TMD}$ for selectively transporting MgATP, we believe that not having an acidic residue at position 190 in AAC could partially explain why AAC has low selectivity for MgATP.

In conclusion, we have identified an acidic residue inside the cavity of the SCaMC carrier domain responsible for both MgATP binding and the strong selectivity for MgATP over ATP. Mitochondrial carriers are relatively small solute transporters with similar molecular architecture. It is remarkable that these similar structures demonstrate exquisite selectivity for substrates with subtle differences, and the selectivity of the metal-complexed ATP by SCaMC is just one of the many examples in the large family of mitochondrial carriers. Structural investigations to understand the mechanism of substrate selectivity have been extremely challenging due to the weak substrate interactions. Our study demonstrates the versatile use of NMR-based titration experiments in identifying residues involved in substrate-transporter interactions. We believe that this approach, in combination with functional mutagenesis, will be applicable to many other transporters for investigating substrate binding and selectivity.

EXPERIMENTAL PROCEDURES

Sample Preparation

A gene encoding residues 186–477 of human SCaMC with a C-terminal 6xHis-tag was cloned into pET21a expression vector. The plasmid containing the protein insertion was transformed into *E. coli* BL21 (DE3) (New England Biolabs) expression strain. The cells were grown at 37°C in M9 minimal media until OD_{600} reached 0.7–0.8. Isopropyl β-D-1-thiogalactopyranoside was then added to a final concentration 0.5 mM to induce the protein expression. The cells were harvested after incubation at 37°C for 3 hr and resuspended in 50 mM Tris-HCl (pH 8.0) and 200 mM NaCl. The cells were disrupted by a homogenizer, followed by centrifugation at 40,000 × *g* for 30 min at 4°C to remove the supernatant. The SCaMC$_{TMD}$-containing inclusion bodies were collected and solubilized in 20 mM HEPES (pH 7.5), 150 mM NaCl, 3 M GdHCl, 1% Triton X-100, and 5 mM β-mercaptoethanol. The resulting solution was applied to an Ni-NTA column, and subsequently refolded on column by exchanging the denaturing buffer with buffer containing 6 mM DPC detergent. The refolded protein was then passed through the Superdex-200 (GE healthcare) size-exclusion column and eluted as monomers at molecular weight ~75 kDa, which is consistent with the total molecular weight of the complex (34 kDa SCaMC$_{TMD}$ plus ~40 kDa DPC micelle). A typical NMR sample consists of 0.4–1 mM SCaMC$_{TMD}$ in the NMR buffer (20 mM MES, 60 mM DPC [pH 6.5]). The mutants D361Y, D361A, and D374A were expressed, purified, and refolded with the same procedure as for the WT.

Table 2. Transport Activities of WT SCaMC$_{TMD}$ and Its Mutants

		ATP	MgATP	MgATP/ATP
Empty	mean[a]	15.5	335.2	
	SD[b]	7.91	13.94	
WT	mean	8,890.6	38,857.6	4.4
	SD	257.85	775.39	0.06
D361Y	mean	3,707.3	4,129.3	1.1
	SD	22.93	69.56	0.01
D374A	mean	4,585.6	13,145.6	2.9
	SD	80.19	66.50	0.04

[a]Mean value of three replicate measurements.
[b]SDs calculated from three replicate measurements.

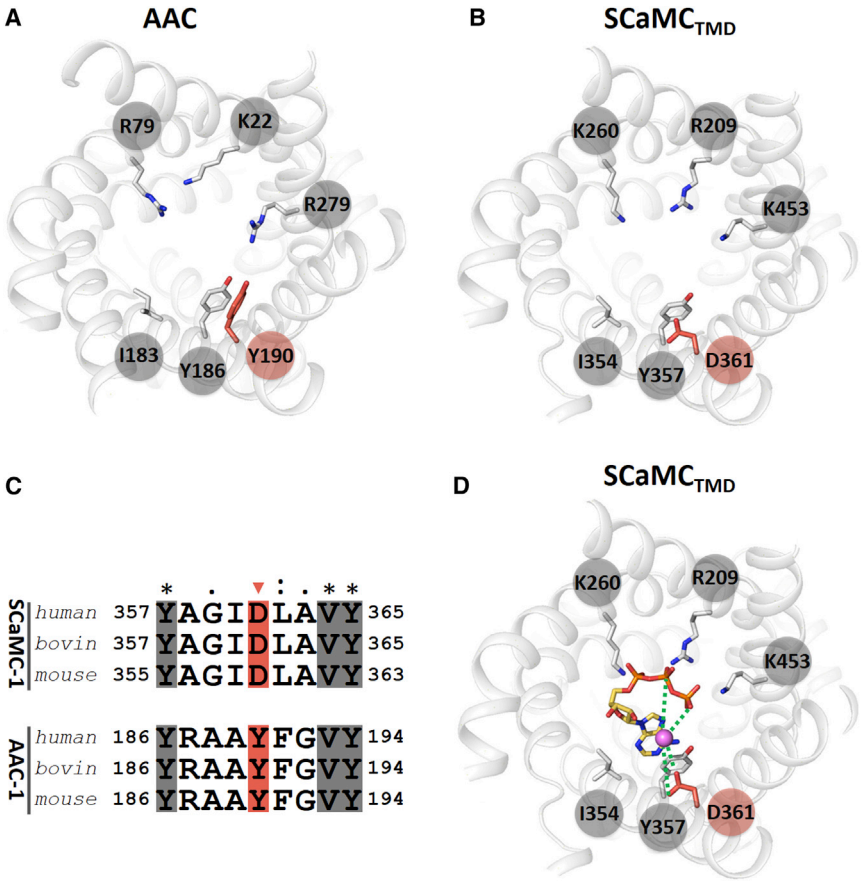

Figure 5. A Proposed Model of MgATP Binding to SCaMC$_{TMD}$

(A and B) Comparison between the cavities of AAC and SCaMC$_{TMD}$ showing their overall similarity, as well as the difference between Y190 in AAC and D361 in SCaMC$_{TMD}$ (highlighted in red).

(C) Sequence alignment between SCaMC$_{TMD}$ and AAC in the region around D361 in SCaMC$_{TMD}$ and Y190 in AAC, showing that these two regions are conserved in SCaMC and AAC. Residues strictly conserved in both AAC and SCaMC$_{TMD}$ are indicated by asterisks and shaded in grey; partially conserved residues are indicated by colons; and much less conserved residues by dots; D361 in SCaMC$_{TMD}$ and Y190 in AAC are indicated by red arrowhead and highlighted in red.

(D) Proposed model illustrating how MgATP could bind to SCaMC$_{TMD}$. In this model, ATP (shown as yellow sticks) interacts with the three basic residues as in AAC, and Mg^{2+} (shown as purple sphere) is coordinated between D361 and the ATP phosphate groups.

NMR Resonance Assignment

All NMR experiments were conducted at 30°C. Sequence-specific assignment of backbone $^{1}H^{N}$, ^{15}N, $^{13}C^{\alpha}$, $^{13}C^{\beta}$, and $^{13}C'$ resonances was accomplished using 3D TROSY-based HNCA, HN(CO)CA, HNCACB, HN(CO)CACB, HN(CA)CO, and HNCO experiments (Kay et al., 1989; Pervushin et al., 1997). In addition, the assignments were validated using a 3D (H^{N}, H^{N})-HSQC-NOESY-TROSY spectrum with ^{15}N, ^{15}N, and $^{1}H^{N}$ evolution in the t_1, t_2, and t_3 dimensions, respectively, recorded with NOE mixing time of 250 ms. These experiments were performed using a 0.8-mM *U*-[^{15}N, ^{13}C, ^{2}H]SCaMC$_{TMD}$ sample at 30°C on a 600-MHz Bruker spectrometer equipped with a cryogenic TXI probe. The NMR spectra were processed using NMRPipe (Delaglio et al., 1995), and analyzed using XEASY (Bartels et al., 1995) and CcpNmr (Vranken et al., 2005).

NMR-Based Titration Experiments

NMR titrations of 500 µl of 0.2 mM [^{15}N]SCaMC$_{TMD}$ sample with 100 µl MgATP, ATP, and free Mg^{2+} stock solution (100 mM in NMR buffer) were performed at 303 K on a 14-T Bruker spectrometer operating at 599.702 and 60.774 MHz for ^{1}H and ^{15}N, respectively. 3D TROSY HNCO spectra were acquired to follow the chemical shift perturbations of MgATP during titrations. A series of 0-, 25-, 50-, 75-, and 100-µl MgATP/ATP/Mg^{2+} stock solutions (100 mM in NMR buffer) were added to a 500-µl 0.4 mM *U*-[^{15}N, ^{13}C, ^{2}H]SCaMC$_{TMD}$ sample. At each substrate concentration point the $^{1}H^{N}$, ^{15}N, and $^{13}C'$ chemical shift changes induced by substrate binding were processed by NMRPipe and analyzed by CcpNmr. The combined chemical shift differences ($\Delta\delta_{comb}$) were calculated for each residue using the formula (Schumann et al., 2007)

$$\Delta\delta^{i}_{comb} = \sqrt{\left(\omega_H \Delta\delta^{i}_{H}\right)^2 + \left(\omega_N \Delta\delta^{i}_{N}\right)^2}, \quad \text{(Equation 2)}$$

where $\Delta\delta_H$ and $\Delta\delta_N$ are chemical shift perturbations (in ppm) with respect to the ^{1}H and ^{15}N chemical shift, and $\omega_H = 1.00$, and $\omega_N = 0.15$ are normalization factors.

The same *U*-[^{15}N, ^{13}C, ^{2}H]SCaMC$_{TMD}$ sample described above was used for measuring displacement of the paramagnetic MnATP by the non-paramagnetic MgATP. The MnATP was first added to the NMR sample to final concentration of 1.25 mM. At this concentration, a subset of resonances was completely broadened in the 3D TROSY HNCO spectra. The NMR sample with 1.25 mM MnATP was then titrated with increasing amounts of MgATP using a 100-mM MgATP stock solution in the NMR buffer. The 3D TROSY HNCO spectra were recorded on addition of 25, 50, 75, 100, and 150 µl of MgATP stock. The peak heights at each MgATP concentration were determined using the CcpNmr software to monitor the recovery of resonances as MnATP were displaced by MgATP. A 0.5-mM ^{15}N-labeled sample was used for measuring displacement of the paramagnetic Mn^{2+} by the non-paramagnetic Mg^{2+}. The 2D ^{1}H-^{15}N TROSY-HSQC spectra were recorded on addition of 1.25 mM $MnCl_2$ and 5, 10, 15, 20, and 30 mM $MgCl_2$. The peaks heights at each $MnCl_2$ and $MgCl_2$ concentration were also determined using the CcpNmr software.

3D Structure Modeling

The 3D structural model of SCaMC$_{TMD}$ was built based on the sequence alignment shown in Figure 1D and the crystal structure of AAC (PDB: 1OKC) using the program Modeller 9.

Proteoliposome Assay

Nucleotide transport activity of SCaMC$_{TMD}$ was measured using liposomes consisting of 1,2-dioleoyl-*sn*-glycero-3-phosphocholine (DOPC), 1,2-dioleoyl-*sn*-glycero-3-phospho-(1′-rac-glycerol) (DOPG), 1,2-dioleoyl-*sn*-glycero-3-phosphoethanolamine (DOPE), and 14:0 1,1′,2,2′-tetra-(9*Z*-octadecenoyl) cardiolipin (CL). To reconstitute SCaMC$_{TMD}$ into liposomes, a lipid solution with lipid composition of DOPC/DOPG/DOPE/CL = 20:5:1:1 (molar ratio) was made by dissolving the lipids in buffer A (20 mM HEPES, 20 mM phosphate buffer [pH 7.8], 100 mM NaCl) with 10% detergent (1:1 mass ratio of decyl maltoside/octyl glucoside) to a total lipid concentration of 20 mg/ml. A protein sample (0.5 mM SCaMC$_{TMD}$) was mixed with the lipid solution at a 1:200 protein/lipid ratio and then diluted 20-fold with buffer A to a lipid concentration of 1 mg/ml. Detergent removal was performed twice on a PD-10 desalting column pre-equilibrated with buffer A. The external and internal buffer was the same for the proteoliposome and thus contained the same concentration of Pi. The resulting proteoliposome was stable for 2 days at room temperature.

Empty liposomes without the addition of protein were prepared in the same way as for a negative control.

To measure the translocation activity, ATP or MgATP was dissolved in buffer A and added into external buffer to a final concentration of 20 mM. Reactions started upon the addition of substrate and terminated with an immediate removal of external substrates after 5 min by passing through PD-10 desalting columns pre-equilibrated with buffer B (20 mM HEPES [pH 7.8], 140 mM NaCl) two times. The amount of ATP transported into proteoliposome was detected by luciferase/luciferin ATP determinant assay (Invitrogen) as described by the manual. In general, a standard reaction solution containing 1.25 μg/ml firefly luciferase and 0.5 mM D-luciferin was made. A 10-μl sample and 100 μl of standard reaction buffer was mixed in a white opaque 96-well microplate followed by immediate detection of luminescence with a spectraMax M5 (Molecular Devices).

SUPPLEMENTAL INFORMATION

Supplemental Information includes seven figures and can be found with this article online at http://dx.doi.org/10.1016/j.str.2015.06.004.

ACKNOWLEDGMENTS

We thank Lingyu Du, Bin Wu, Meng Wu, and Fangfang Zhong for technical assistance and insightful discussions. This work was supported by the Strategic Priority Research Program of the Chinese Academy of Sciences, grant no. XDB08030301, NIH Grant GM094608 (to J.J.C.), and National Natural Science Foundation of China grant no. 31270905 (to Z.J.L).

Received: March 3, 2015
Revised: May 28, 2015
Accepted: June 4, 2015
Published: July 9, 2015

REFERENCES

Aprille, J.R. (1988). Regulation of the mitochondrial adenine nucleotide pool size in liver: mechanism and metabolic role. FASEB J. *2*, 2547–2556.

Austin, J., and Aprille, J.R. (1984). Carboxyatractyloside-insensitive influx and efflux of adenine nucleotides in rat liver mitochondria. J. Biol. Chem. *259*, 154–160.

Barrett, P.J., Song, Y., Van Horn, W.D., Hustedt, E.J., Schafer, J.M., Hadziselimovic, A., Beel, A.J., and Sanders, C.R. (2012). The amyloid precursor protein has a flexible transmembrane domain and binds cholesterol. Science *336*, 1168–1171.

Bartels, C., Xia, T.H., Billeter, M., Guntert, P., and Wuthrich, K. (1995). The program XEASY for computer-supported NMR spectral analysis of biological macromolecules. J. Biomol. NMR *6*, 1–10.

Berardi, M.J., and Chou, J.J. (2014). Fatty acid flippase activity of UCP2 is essential for its proton transport in mitochondria. Cell Metab. *20*, 541–552.

Berardi, M.J., Shih, W.M., Harrison, S.C., and Chou, J.J. (2011). Mitochondrial uncoupling protein 2 structure determined by NMR molecular fragment searching. Nature *476*, 109–113.

Cathala, G., and Brunel, C. (1975). Bovine kidney alkaline phosphatase. Catalytic properties, subunit interactions in the catalytic process, and mechanism of Mg^{2+} stimulation. J. Biol. Chem. *250*, 6046–6053.

Cavero, S., Traba, J., Del Arco, A., and Satrustegui, J. (2005). The calcium-dependent ATP-Mg/Pi mitochondrial carrier is a target of glucose-induced calcium signalling in Saccharomyces cerevisiae. Biochem. J. *392*, 537–544.

Chen, X.J. (2004). Sal1p, a calcium-dependent carrier protein that suppresses an essential cellular function associated with the Aac2 isoform of ADP/ATP translocase in Saccharomyces cerevisiae. Genetics *167*, 607–617.

Dehez, F., Pebay-Peyroula, E., and Chipot, C. (2008). Binding of ADP in the mitochondrial ADP/ATP carrier is driven by an electrostatic funnel. J. Am. Chem. Soc. *130*, 12725–12733.

del Arco, A., and Satrustegui, J. (2004). Identification of a novel human subfamily of mitochondrial carriers with calcium-binding domains. J. Biol. Chem. *279*, 24701–24713.

Delaglio, F., Grzesiek, S., Vuister, G.W., Zhu, G., Pfeifer, J., and Bax, A. (1995). NMRPipe: a multidimensional spectral processing system based on UNIX pipes. J. Biomol. NMR *6*, 277–293.

Fiermonte, G., De Leonardis, F., Todisco, S., Palmieri, L., Lasorsa, F.M., and Palmieri, F. (2004). Identification of the mitochondrial ATP-Mg/Pi transporter. Bacterial expression, reconstitution, functional characterization, and tissue distribution. J. Biol. Chem. *279*, 30722–30730.

Fiore, C., Trezeguet, V., Le Saux, A., Roux, P., Schwimmer, C., Dianoux, A.C., Noel, F., Lauquin, G.J., Brandolin, G., and Vignais, P.V. (1998). The mitochondrial ADP/ATP carrier: structural, physiological and pathological aspects. Biochimie *80*, 137–150.

Garlid, K.D., Orosz, D.E., Modriansky, M., Vassanelli, S., and Jezek, P. (1996). On the mechanism of fatty acid-induced proton transport by mitochondrial uncoupling protein. J. Biol. Chem. *271*, 2615–2620.

Guth, J.H., and Burris, R.H. (1983). The role of Mg^{2+} and Mn^{2+} in the enzyme-catalysed activation of nitrogenase Fe protein from *Rhodospirillum rubrum*. Biochem. J. *213*, 741–749.

Hsu, M., and Berg, P. (1978). Altering the specificity of restriction endonuclease: effect of replacing Mg^{2+} with Mn^{2+}. Biochemistry *17*, 131–138.

Huss, J.M., and Kelly, D.P. (2005). Mitochondrial energy metabolism in heart failure: a question of balance. J. Clin. Invest. *115*, 547–555.

Joyal, J.L., and Aprille, J.R. (1992). The ATP-Mg/Pi carrier of rat liver mitochondria catalyzes a divalent electroneutral exchange. J. Biol. Chem. *267*, 19198–19203.

Kay, L.E., Torchia, D.A., and Bax, A. (1989). Backbone dynamics of proteins as studied by ^{15}N inverse detected heteronuclear NMR spectroscopy: application to staphylococcal nuclease. Biochemistry *28*, 8972–8979.

Klingenberg, M. (2008). The ADP and ATP transport in mitochondria and its carrier. Biochim. Biophys. Acta *1778*, 1978–2021.

Kunji, E.R., and Robinson, A.J. (2006). The conserved substrate binding site of mitochondrial carriers. Biochim. Biophys. Acta *1757*, 1237–1248.

Nosek, M.T., Dransfield, D.T., and Aprille, J.R. (1990). Calcium stimulates ATP-Mg-Pi carrier activity in rat liver mitochondria. J. Biol. Chem. *265*, 8444–8450.

Nury, H., Dahout-Gonzalez, C., Trézéguet, V., Lauquin, G.J.M., Brandolin, G., and Pebay-Peyroula, E. (2006). Relations between structure and function of the mitochondrial ADP/ATP carrier. Annu. Rev. Biochem. *75*, 713–741.

Ohshima, N., Yamashita, S., Takahashi, N., Kuroishi, C., Shiro, Y., and Takio, K. (2008). Escherichia coli cytosolic glycerophosphodiester phosphodiesterase (UgpQ) requires Mg^{2+}, Co^{2+}, or Mn^{2+} for its enzyme activity. J. Bacteriol. *190*, 1219–1223.

Palmieri, F. (2008). Diseases caused by defects of mitochondrial carriers: a review. Biochim. Biophys. Acta *1777*, 564–578.

Pebay-Peyroula, E., Dahout-Gonzalez, C., Kahn, R., Trézéguet, V., Lauquin, G.J., and Brandolin, G. (2003). Structure of mitochondrial ADP/ATP carrier in complex with carboxyatractyloside. Nature *426*, 39–44.

Pervushin, K., Riek, R., Wider, G., and Wuthrich, K. (1997). Attenuated T2 relaxation by mutual cancellation of dipole-dipole coupling and chemical shift anisotropy indicates an avenue to NMR structures of very large biological macromolecules in solution. Proc. Natl. Acad. Sci. USA *94*, 12366–12371.

Pollak, J.K., and Sutton, R. (1980). The transport and accumulation of adenine nucleotides during mitochondrial biogenesis. Biochem. J. *192*, 75–83.

Ruprecht, J.J., Hellawell, A.M., Harding, M., Crichton, P.G., McCoy, A.J., and Kunji, E.R. (2014). Structures of yeast mitochondrial ADP/ATP carriers support a domain-based alternating-access transport mechanism. Proc. Natl. Acad. Sci. USA *111*, E426–E434.

Satrústegui, J., Pardo, B., and del Arco, A. (2007). Mitochondrial transporters as novel targets for intracellular calcium signaling. Physiol. Rev. *87*, 29–67.

Schild, L., Blair, P.V., Davis, W.I., and Baugh, S. (1999). Effect of adenine nucleotide pool size in mitochondria on intramitochondrial ATP levels. Biochim. Biophys. Acta *1413*, 14–20.

Schumann, F.H., Riepl, H., Maurer, T., Gronwald, W., Neidig, K.P., and Kalbitzer, H.R. (2007). Combined chemical shift changes and amino acid specific chemical shift mapping of protein-protein interactions. J. Biomol. NMR *39*, 275–289.

Shen, Y., Delaglio, F., Cornilescu, G., and Bax, A. (2009). TALOS+: a hybrid method for predicting protein backbone torsion angles from NMR chemical shifts. J. Biomol. NMR *44*, 213–223.

Sounier, R., Bellot, G., and Chou, J.J. (2015). Mapping conformational heterogeneity of mitochondrial nucleotide transporter in uninhibited states. Angew. Chem. Int. Ed. Engl. *54*, 2436–2441.

Traba, J., Del Arco, A., Duchen, M.R., Szabadkai, G., and Satrustegui, J. (2012). SCaMC-1 promotes cancer cell survival by desensitizing mitochondrial permeability transition via ATP/ADP-mediated matrix Ca(2+) buffering. Cell Death Differ. *19*, 650–660.

Vranken, W.F., Boucher, W., Stevens, T.J., Fogh, R.H., Pajon, A., Llinas, M., Ulrich, E.L., Markley, J.L., Ionides, J., and Laue, E.D. (2005). The CCPN data model for NMR spectroscopy: development of a software pipeline. Proteins *59*, 687–696.

Webb, B., and Sali, A. (2014). Comparative protein structure modeling using MODELLER. Curr. Protoc. Bioinformatics *47*, 5 6 1–5 6 32.

Yang, Q., Bruschweiler, S., and Chou, J.J. (2014). A self-sequestered calmodulin-like Ca(2)(+) sensor of mitochondrial SCaMC carrier and its implication to Ca(2)(+)-dependent ATP-Mg/P(i) transport. Structure *22*, 209–217.

Zhang, M., Le Clair, S.V., Huang, R., Ahuja, S., Im, S.C., Waskell, L., and Ramamoorthy, A. (2015). Insights into the role of substrates on the interaction between cytochrome b5 and cytochrome P450 2B4 by NMR. Sci. Rep. *5*, 8392.

Structure, Volume *23*

Supplemental Information

Molecular Basis of MgATP Selectivity of the Mitochondrial SCaMC Carrier

Changqing Run, Qin Yang, Zhijun Liu, Bo OuYang, and James J. Chou

Supplemental Information

Molecular Basis of MgATP Selectivity of the Mitochondrial SCaMC Carrier

Changqing Run[1, 2], Qin Yang[3], Zhijun Liu[1], Bo OuYang[1, 2]*, James J. Chou[1, 2, 3]*

Supplemental Figures

Figure S1 Sequence Alignment between AAC and $SCaMC_{TMD}$ for showing the conserved residues between the two nucleotide transporters. *Relates to Figure 1, to show the similarity between AAC and SCaMC.*

Figure S2 Comparison of the effects of MgATP, ATP and Mg^{2+} on $SCaMC_{TMD}$ chemical shifts. *Relates to Figure 2 to show that MgATP and ATP are substrates of SCaMC whereas Mg^{2+} is not.*

Figure S3 Estimation of MgATP binding affinity using chemical shift titration data. *Relates to Figure 2 & 3, to show that the binding affinity calculated from chemical shift changes and MnATP/MgATP broadening/recovery are consistent.*

Figure S4 The Mn^{2+}/Mg^{2+} titration showing the inability of Mg^{2+} cation alone to displace the paramagnetic Mn^{2+}. *Relates to Figure 3, to show that MgATP induced specific displacement of MnATP is not due to non-specific binding of Mg^{2+} cations.*

Figure S5 The nucleotide transport activity of $SCaMC_{TMD}$ showing a much higher selectivity for MgATP over ATP. *Relates to Figure 4, to show that the liposome assay functioned as expected.*

Figure S6 Comparison of the NMR spectra of the WT and mutant $SCaMC_{TMD}$ showing negligible effect of the mutations on the transporter structure. *Relates to Figure 4, to show that the point mutations have essentially no effect on the protein conformation.*

Figure S7 The inability of $SCaMC_{TMD}$ to bind MgATP by mutation of D361A. *Relates to Figure 3 & 4, to show that D361 is the key residue for MgATP binding.*

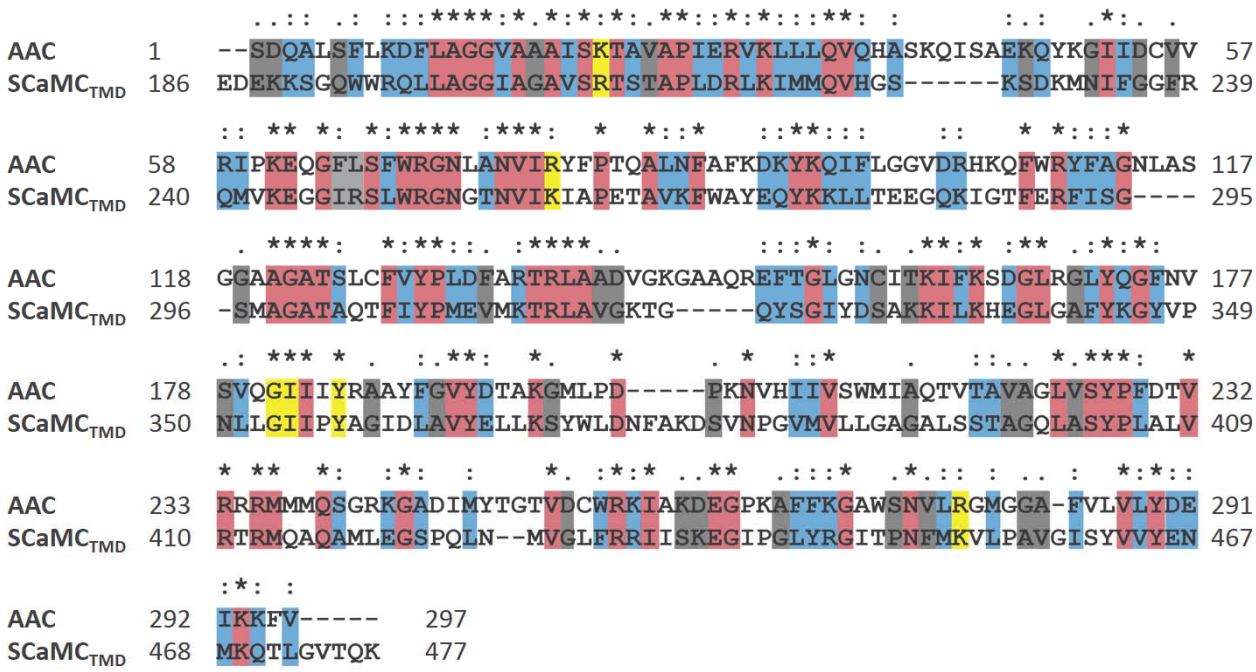

Figure S1. Sequence alignment between AAC and SCaMC$_{TMD}$ for showing the conserved residues between the two nucleotide transporters. Residues strictly conserved in both AAC and SCaMC$_{TMD}$ are indicated by asterisks '*' and shaded in red; partially conserved are indicated by colons ':' and shaded in blue; much less conserved are indicated by dots '.' and shaded in gray. The six residues involved in ATP binding are highlighted in yellow.

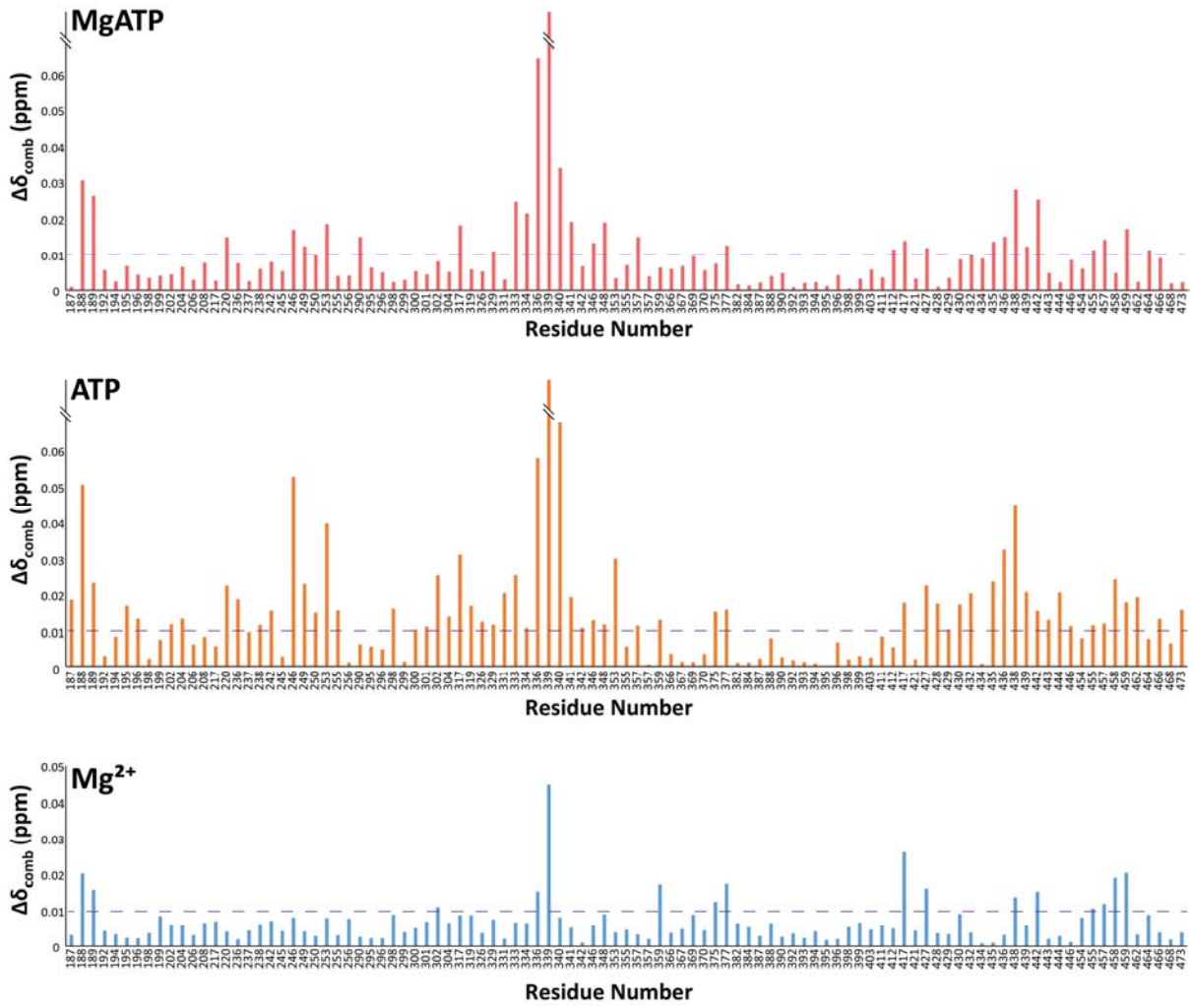

Figure S2. Comparison of the effects of MgATP, ATP and Mg^{2+} on $SCaMC_{TMD}$ chemical shifts. Spectra were recorded using a 0.2 mM ^{15}N labeled sample without substrates and with the addition of 16.7 mM MgATP (upper panel), 16.7 mM ATP (middle panel) or 16.7 mM Mg^{2+} (lower panel). Only resolved peaks are depicted here. The dashed lines correspond to 0.01 ppm.

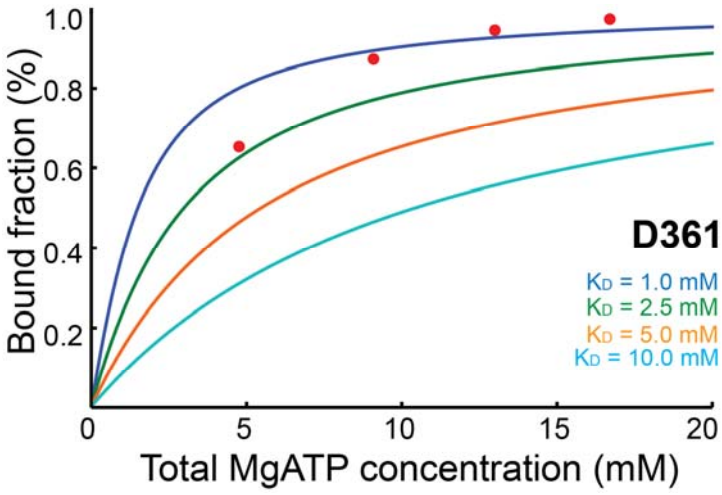

Figure S3. Estimation of MgATP binding affinity using chemical shift titration data. Binding affinity simulation curves for 0.4 mM $SCaMC_{TMD}$ titrated with substrates with affinities of 1.0 mM, 2.5 mM, 5.0 mM and 10 mM are colored in blue, green, orange and cyan, respectively. Following equation was used for calculating the MgATP bound fraction of $SCaMC_{TMD}$ $\frac{[PS]}{[P_{total}]} = \frac{([P_{total}]+[S_{total}]+Kd) \pm \sqrt{([P_{total}]+[S_{total}]+Kd)^2 - 4[P_{total}][S_{total}]}}{2[P_{total}]}$. In this equation, P_{total} represent the total amount of protein used. S_{total} represents the total amount of substrate titrated. PS represents the protein/substrate complex. The X-axis is the total substrate concentration used for titration. The y-axis indicates the theoretical percentage of bound fraction. A serial of 0, 4.8, 9.1, 13.0 and 16.7 mM MgATP were titrated into 0.4 mM $SCaMC_{TMD}$ under our NMR titration condition. The corresponding bound fractions as measured from 2D chemical shift for residue D361 were plotted as red dots, which suggest a binding affinity around 1.5 mM.

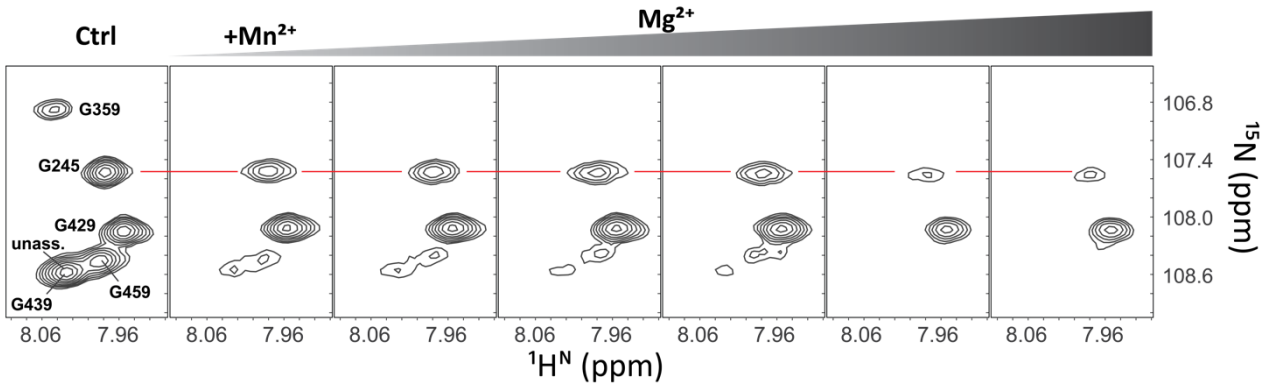

Figure S4. The Mn^{2+}/Mg^{2+} titration showing the inability of Mg^{2+} cation alone to displace the paramagnetic Mn^{2+}. The region from the 2D ^{1}H-^{15}N TROSY-HSQC spectra, recorded using a 0.5 mM ^{15}N labeled sample, is the same as in Fig. 3A&C. The first panel shows peaks in the absence of Mn^{2+} and Mg^{2+}. The second panel shows broadening of peaks in the presence of 1.25 mM Mn^{2+}. Panels 3 to 7 are spectra recorded at increasing concentrations of Mg^{2+}: 5, 10, 15, 20 and 30 mM.

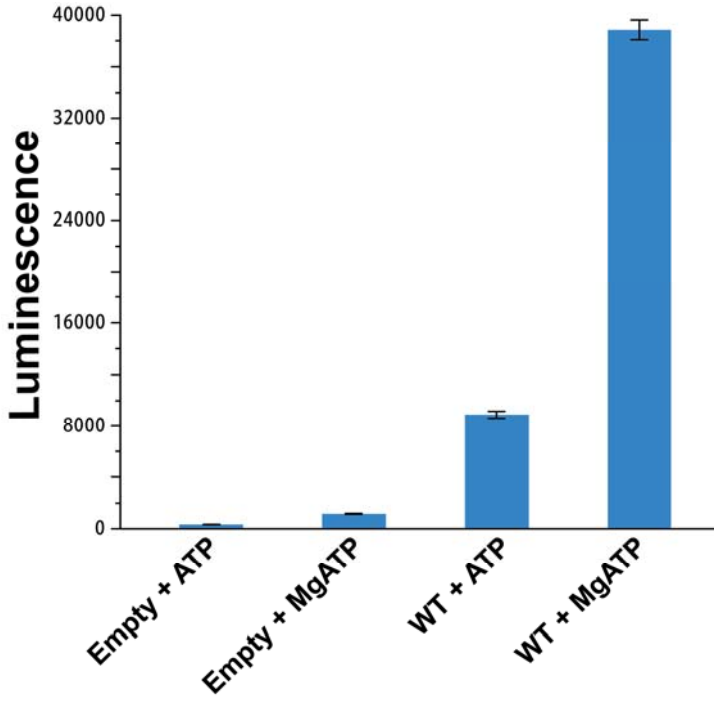

Figure S5. The nucleotide transport activity of $SCaMC_{TMD}$ showing a much higher selectivity for MgATP over ATP. The activities were measuring using the proteoliposome assay depicted in Fig. 4A. In the duration of 5 minutes, $SCaMC_{TMD}$ transports about 4.5 times as much MgATP as ATP. Error bars are ± one s.t.d. values determined from 3 repeat measurements.

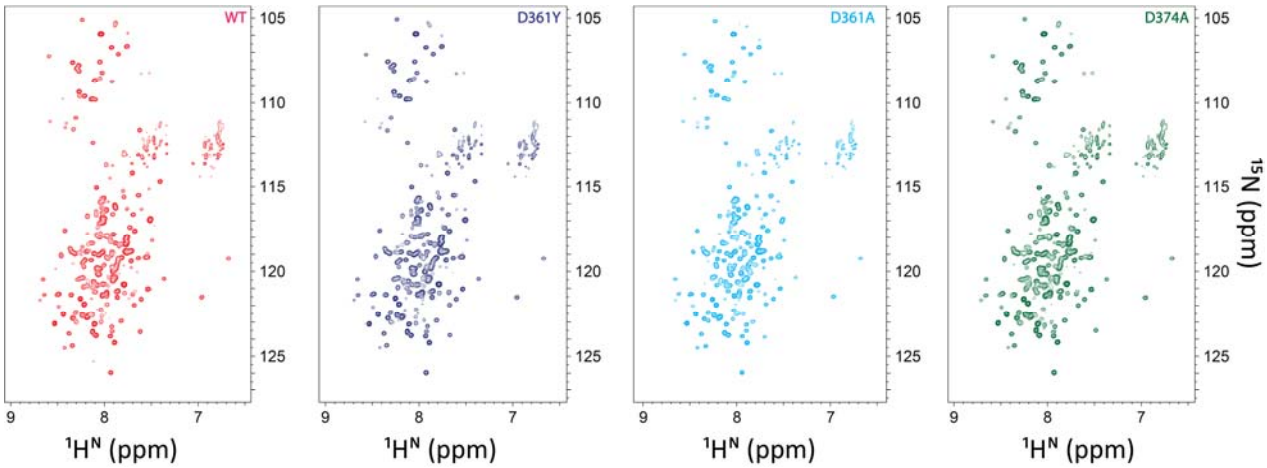

Figure S6. Comparison of the NMR spectra of the WT and mutant $SCaMC_{TMD}$ showing negligible effect of the mutations on the overall transporter structure. The 2D ^1H-^{15}N TROSY-HSQC spectra of the WT, D361Y, D361A and D374A mutants were recorded using 0.5 mM ^{15}N labeled protein in the same buffer condition.

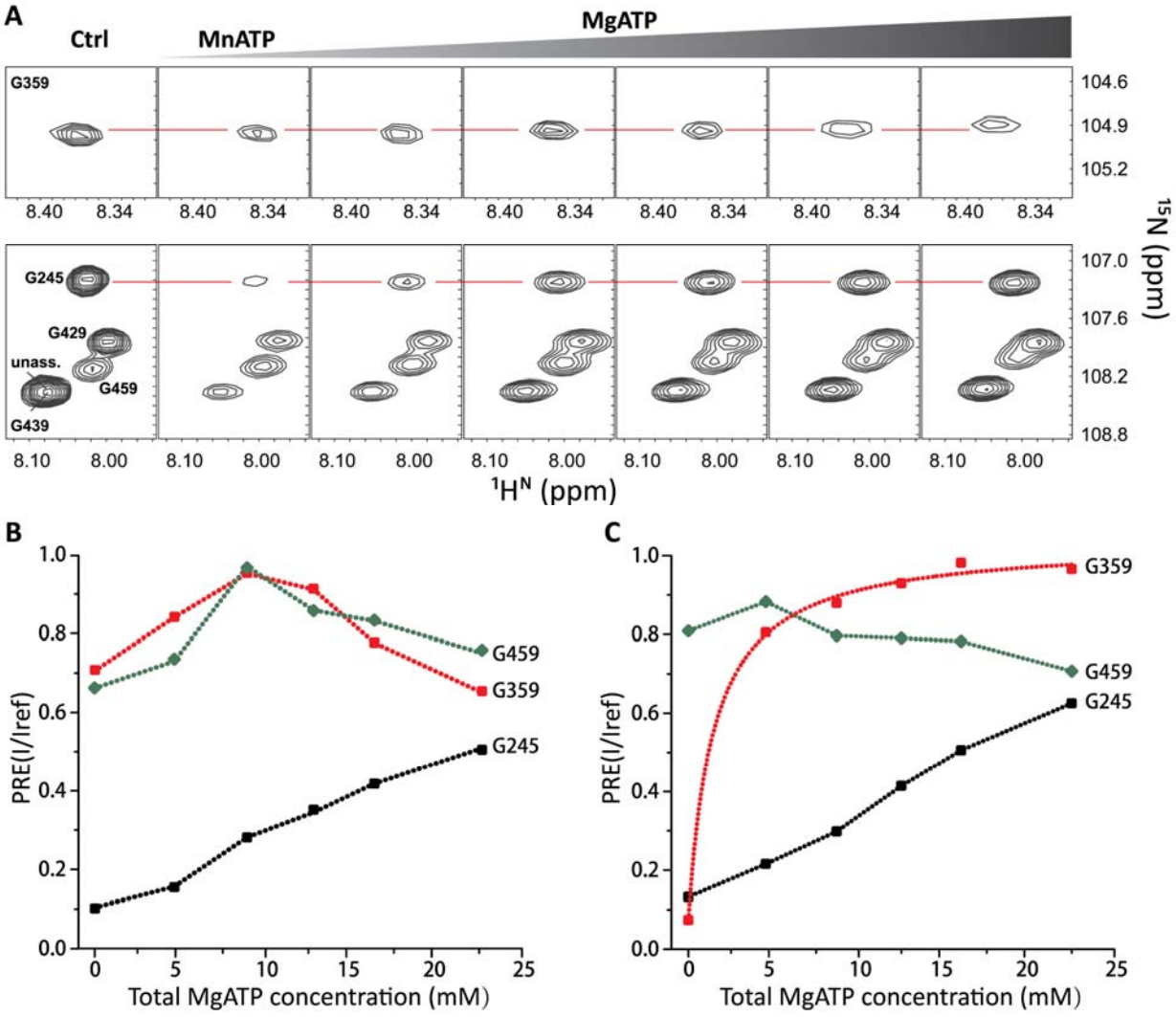

Figure S7. The D361A mutation abrogates the ability of SCaMC$_{TMD}$ to bind MgATP

(A) The MnATP/MgATP titration showing the inability of MgATP to displace MnATP for the D361A mutant. The region from the 2D ^{1}H-^{15}N TROSY-HSQC spectra, recorded using a 0.5 mM *U*-[^{15}N, ^{13}C, ^{2}H]-labelled sample, contains the same peaks as in Fig. 3A&C. The first panel shows peaks in the absence of MnATP and MgATP. The second panel shows broadening of peaks in the presence of 1.25 mM MnATP. Panels 3 to 7 are spectra recorded at increasing concentrations of 4.5, 8.69, 12.5, 16.0 and 22.2 mM MgATP.

(B) Plots of PRE (normalized peak intensity) vs. MgATP concentration for the D361A mutant for the residues labeled in (A).

(C) The same plots as in (B) for the WT SCaMC$_{TMD}$.